

Research
Robotics—Article

A High-Precision US-Guided Robot-Assisted HIFU Treatment System for Breast Cancer



Tianhan Tang^a, Takashi Azuma^{b,*}, Toshihide Iwahashi^a, Hideki Takeuchi^a, Etsuko Kobayashi^a, Ichiro Sakuma^a

^aGraduate School of Engineering, The University of Tokyo, Tokyo 113-8656, Japan

^bGraduate School of Medicine, The University of Tokyo, Tokyo 113-8654, Japan

ARTICLE INFO

Article history:

Received 31 March 2017

Revised 21 December 2017

Accepted 10 July 2018

Available online 17 July 2018

Keywords:

HIFU

Breast cancer

US-guided navigation

Medical robotics

Accuracy evaluation

ABSTRACT

Breast cancer is the most commonly diagnosed cancer in women. A strong treatment candidate is high-intensity focused ultrasound (HIFU), a non-invasive therapeutic method that has already demonstrated its promise. To improve the precision and lower the cost of HIFU treatment, our group has developed an ultrasound (US)-guided, five-degree-of-freedom (DOF), robot-assisted HIFU system. We constructed a fully functional prototype enabling easy three-dimensional (3D) US image reconstruction, target segmentation, treatment path generation, and automatic HIFU irradiation. The position was calibrated using a wire phantom and the coagulated area was assessed on heterogeneous tissue phantoms. Under the US guidance, the centroids of the HIFU-ablated area deviated by less than 2 mm from the planned treatment region. The overshoot around the planned region was well below the tolerance of clinical usage. Our system is considered to be sufficiently accurate for breast cancer treatment.

© 2018 THE AUTHORS. Published by Elsevier LTD on behalf of Chinese Academy of Engineering and Higher Education Press Limited Company. This is an open access article under the CC BY-NC-ND license (<http://creativecommons.org/licenses/by-nc-nd/4.0/>).

1. Introduction

Breast cancer is the most common cancer in women worldwide [1], and the most frequently diagnosed cancer in women throughout Japan [2]. Therefore, it poses a major threat to quality of life.

High-intensity focused ultrasound (HIFU) is a non-invasive, therapeutic ultrasound (US) technology that delivers a precisely focused acoustic beam to a small volume in the body. The high acoustic energy of the HIFU beam causes thermal necrosis of the target tissue. Most beneficially, this technology can selectively destroy deep malignant tissues, with little damage to the overlying and surrounding tissues along the beam path. HIFU is a promising method for treating breast and other types of cancer [3–5]. The concept view of the HIFU treatment for breast cancer is shown in Fig. 1.

To fully exploit the non-invasiveness of HIFU, the HIFU technology should be integrated into the modern image-guided robot-assisted surgical system paradigm. An image-guided robot-assisted system typically comprises three main parts: a medical

imaging system, a medical robot system, and a medical navigation system. The imaging and robot systems extend the functionalities of the surgeon's eyes and hands, respectively, and the navigation system coordinates and associates with the hand-eye system. Therefore, the navigation system is vitally important in a precise surgical treatment.

At present, HIFU navigation tasks are guided by magnetic resonance imaging (MRI). MRI has high spatial resolution and can monitor tissue temperature through the temperature-dependent effects on the proton resonant frequency [6,7]. However, MRI-guided HIFU has several drawbacks. First, the low frame-refresh rate of MRI impedes real-time navigation. Second, the bulk size of MRI is problematic for system integration. Third, the confined space of the MRI gantry limits the possible angles along which the robot system can approach the target region, thereby compromising the treatment delivery and increasing the risk of skin burn. Fourth, the strong magnetic field generated by MRI imposes additional constraints on the robot system. Most of the common robot components cannot be used in close proximity to magnets, so operation near MRI requires special strategies that increase the system complexity [8]. Fifth, the high cost has prevented the popularization of HIFU treatment.

* Corresponding author.

E-mail address: azuma@fel.t.u-tokyo.ac.jp (T. Azuma).

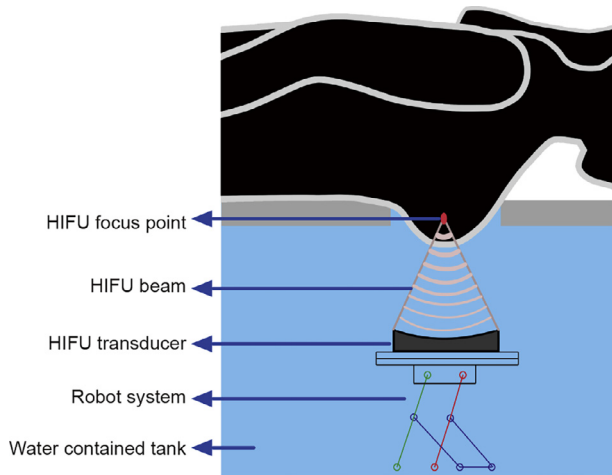


Fig. 1. Concept view of the HIFU treatment for breast cancer.

In contrast, US imaging is a compact, cheap technology with a fast frame-refresh rate. Owing to these features, in addition to its versatility and easy accessibility, US imaging has become an increasingly popular modality in image-guided surgery. However, the conventional US diagnostic system provides only a two-dimensional (2D) image of the target region. To create an accurate three-dimensional (3D) atlas for the HIFU treatment plan, it is preferable to utilize a robot system to collect a stack of 2D US images and reconstruct a 3D US image from the stack. To this end, our group has proposed a US-guided robot-assisted HIFU system as a precise, low-cost breast cancer treatment solution. The ultimate goal is to promote HIFU treatment and improve the quality of life of patients.

Here, we focus on the navigation system of the proposed treatment system. To achieve an effective and accurate HIFU treatment, the navigation system should take the user through the treatment workflow, from image acquisition to treatment execution. The internal functional blocks should include 3D reconstruction of the US images, target definition, and treatment path generation. To obtain the correct spatial relation between the US image space and the robot working space, hand-eye calibration is also necessary. These functions are implemented as subtasks to achieve the main objective. Finally, the overall accuracy of the treatment system should be evaluated.

The remainder of this paper is organized as follows. After overviewing the constitution of our system in Section 2, we detail the development of the US-guided navigation system for HIFU treatment and its evaluation method in Section 3. The experiment results are presented in Section 4. We discuss the results in Section 5, and conclude with Section 6.

2. System overview

2.1. Hardware components of the HIFU system

The system consists of three main parts: a HIFU transducer with an appropriate controller unit that provides the required energy for treatment, a US imaging system (Prosound® F75, Hitachi, Ltd., Tokyo, Japan) that provides the necessary diagnostic information for navigation, and a custom-made five-degree-of-freedom (DOF) parallel-link robot system that manipulates the HIFU transducer and the modified US imaging transducer.

Table 1
Specifications of the HIFU and imaging transducers.

Parameter	HIFU transducer	Imaging transducer
Type	Concave hemispherical	Linear
Number of elements	256	128
Diameter of aperture (mm)	120	—
Geometric focal length (mm)	100	—
Elevation focal length (mm)	—	60
Pitch of element (mm)	—	0.2
Length of element (mm)	—	8
Central frequency (MHz)	2	5
Fractional bandwidth (%)	~50	65
Probe length (mm)	—	30
Probe width (mm)	—	16

The two transducers are configured confocally and fixed on the end-effector of the robot system. The specifications of both transducers are shown in Table 1. The modified imaging transducer has an elevation focal length of 60 mm, which was specifically designed to provide better image resolution at depth than a common commercially available transducer. The five-DOF robot system precisely manipulates the HIFU and imaging transducers to perform the scanning for diagnosis and the positioning for therapy. In conventional US diagnosis, the imaging probe usually contacts the skin surface, and the US attenuation is arrested by coupling gels to ensure good imaging. However, the imaging probe in our system is held by the robot system, not by the physician. Therefore, regular trace scanning with the probe touching the skin is inconvenient. Moreover, if the imaging probe contacts the skin, the focusing of the HIFU beam is impeded. Therefore, in our system design, the imaging probe remains separate from the skin of the patient. The coupling problem is resolved by designing an underwater workspace for our robot system. As the acoustic attenuation coefficient of water is very low ($\sim 0.0022 \text{ dB} \cdot (\text{MHz} \cdot \text{cm})^{-1}$ [9]), we obtained good US images even at 120 mm (the furthest distance between the boundary of the US image and the surface of the imaging probe). Another benefit of not contacting the probe with the skin surface is that the breast does not deform under the scanning process. Breast tissue is very soft; however, provided that the probe remains detached and the 2D real-time US image is readily available during the treatment process, deformation should not be a problem in our system. During the treatment, the patient lies prone on a bed above the water tank, and the breast to be treated is inserted into the workspace. A rubber membrane between the breast and the tank water prevents direct contact between the patient and the water without impeding the US wave propagation.

The overall components and connections of the system are shown in Fig. 2. The first personal computer (PC1) sets the focus data for the HIFU transducer driver. The command is sent through a universal serial bus (USB)-to-universal asynchronous receiver/transmitter (UART) cable. The second personal computer (PC2) coordinates the overall HIFU system. PC2 sets the output level of the HIFU transducer via a USB-to-analog input-output (AIO) unit (provided by Contec Co., Ltd., Osaka, Japan), and receives the 2D US images from the US imaging system through a video grabber with a digital visual interface (DVI)-to-USB 3.0 interface (provided by Epiphan Systems Inc., Ottawa, ON, Canada). PC2 also communicates with the robot controller over a local area network (LAN) cable in order to set and track the pose of the robot. The robot controller is connected to a motor that controls the rotation angle φ (see Section 3.1) by a USB-to-RS-232-C cable. The other four motors are connected to the robot controller through a USB-to-controller area network (CAN) cable.

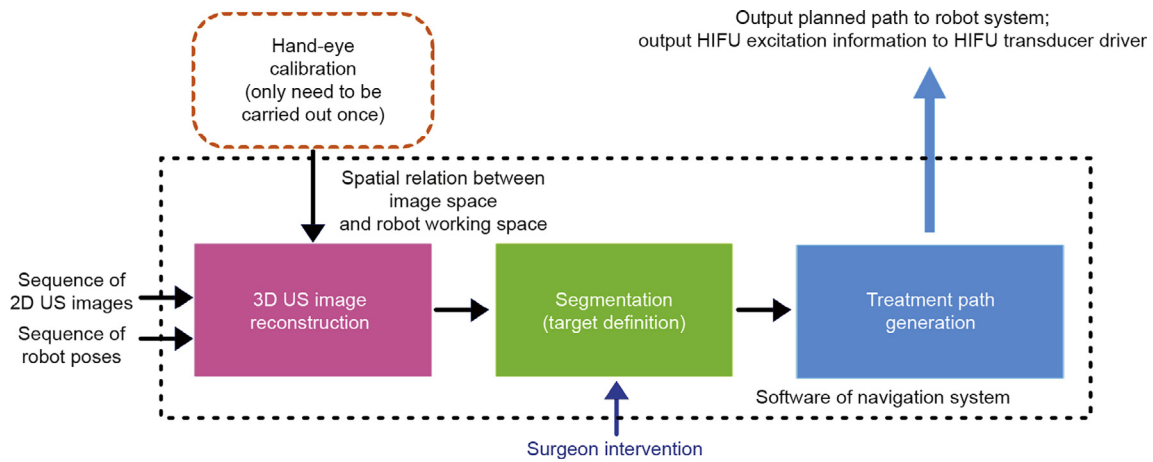


Fig. 3. Block diagram of the navigation system software.

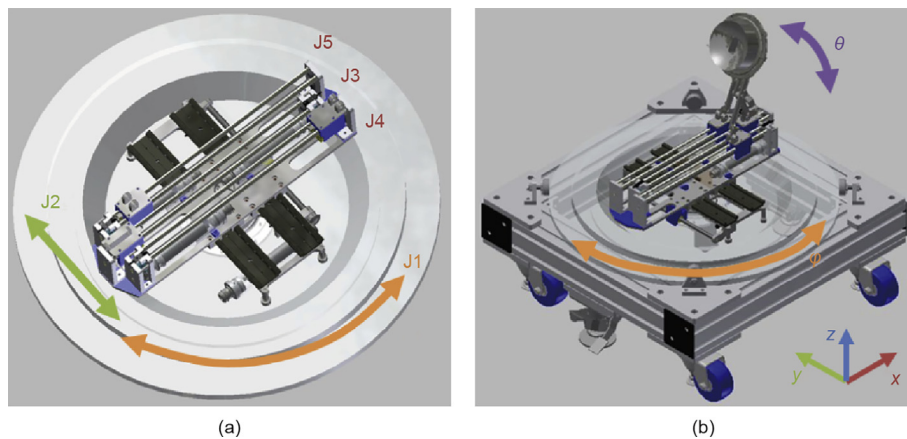


Fig. 4. (a) Input space and (b) output space of the five-DOF robot system.

Table 2

Input shaft specifications of the robot system.

Input shaft	Motion range	Max speed	Precision	Motor resolution
J1	−157° to 243°	200 r.min ^{−1}	±0.004°	36 000 pulse.r ^{−1}
J2	−100 to 100 mm	45.2 mm.s ^{−1}	±50 μm	666.3 nm.pulse ^{−1}
J3	−160 to 180 mm	45.2 mm.s ^{−1}	±50 μm	666.3 nm.pulse ^{−1}
J4	−230 to 110 mm	45.2 mm.s ^{−1}	±50 μm	666.3 nm.pulse ^{−1}
J5	−160 to 180 mm	45.2 mm.s ^{−1}	±50 μm	666.3 nm.pulse ^{−1}

the system (including the water tank) while maintaining the necessary flexibility for various approach angles to the treatment target. Second, in practical breast cancer treatment, it is usually preferable to place the target region near the rotation axis z and set θ such that the HIFU beam is orthogonal to the skin surface. This configuration reduces the risk of skin burn. By using a dedicated motor (J1) to control rotation about the z axis, we can spatially fix the HIFU focus point on the z axis while causing the approaching HIFU beam to rotate about it. This enables efficient treatment while further reducing the risk of skin burn [10]. Third, the parallel links controlling x , z , and θ ensure that when irradiation is performed from an upright and from a side-to-side position,

the z coordinate of the HIFU transducer is low and high, respectively, as is required for the actual treatment.

The joints and links of the robot system are illustrated in Fig. 5. Joints J_{34} and J_{35} are situated at the center of links $A-J_4$ and $B-J_5$, respectively. From the given design parameters (Table 3), we calculated identical x coordinates for J_3 and joint A , and for J'_3 and joint B . The positions of joints J_3 and J'_3 are controlled by shaft J3, while the positions of joints J_4 and J_5 are controlled by shaft J4 and J5, respectively.

The robot system controls the position and orientation of the HIFU focus point by manipulating the HIFU transducer. The spatial information of the focus point (denoted as F in Fig. 5) in the output

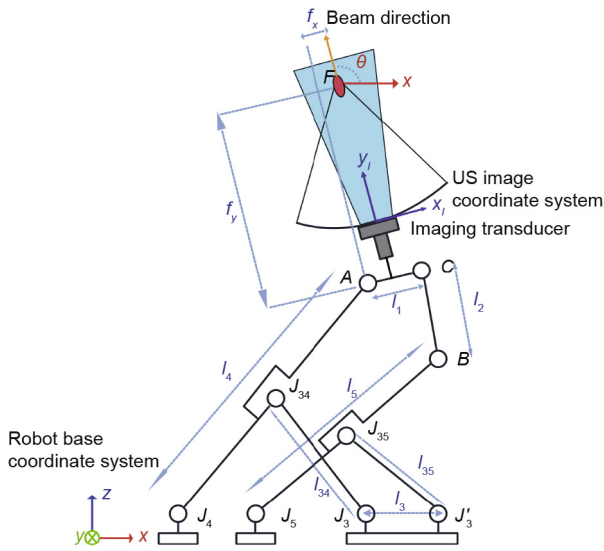


Fig. 5. Joints and links of the robot system.

Table 3
Design parameters of the robot system.

Parameter	Value	Parameter	Value
l_1	80 mm	l_5	200 mm
l_2	80 mm	l_{35}	100 mm
l_3	80 mm	f_x	40 mm
l_4	200 mm	f_y	164 mm
l_{34}	100 mm	Ω	90°

Ω is the angle between the HIFU beam direction and link A–C.

space is specified by the parameter set $(\theta, x, y, z, \varphi)$. The angle between the HIFU beam direction and link A–C is denoted as Ω . The inverse kinematics of the system (i.e., determining the input parameters from the desired output parameters) are given by Eq. (1):

$$\begin{bmatrix} J1 \\ J2 \\ J3 \\ J4 \\ J5 \end{bmatrix} = \begin{bmatrix} \varphi \\ y \\ A_x \\ A_x - \sqrt{l_4^2 - A_z^2} \\ B_x - \sqrt{l_5^2 - B_z^2} \end{bmatrix} \quad (1)$$

where

$$\begin{bmatrix} A_x \\ A_z \end{bmatrix} = \begin{bmatrix} x - \sqrt{f_x^2 + f_y^2} \cdot \cos(\theta - \Omega + \angle FAC) \\ y - \sqrt{f_x^2 + f_y^2} \cdot \sin(\theta - \Omega + \angle FAC) \end{bmatrix} \quad (2)$$

$$\begin{bmatrix} B_x \\ B_z \end{bmatrix} = \begin{bmatrix} J3 + l_3 \\ C_z - \sqrt{l_2^2 - (B_x - C_x)^2} \end{bmatrix} \quad (3)$$

and

$$\begin{bmatrix} C_x \\ C_z \end{bmatrix} = \begin{bmatrix} A_x + l_1 \cdot \cos(\theta - \Omega) \\ A_z + l_1 \cdot \sin(\theta - \Omega) \end{bmatrix} \quad (4)$$

where the subscripts x and z denote the x and z coordinates, respectively, of points A, B, or C in the output space. J1, J2, J3, J4, and J5 in

Eq. (1) are the input values for each of the five shafts. The angle $\angle FAC$ in Eq. (2) was determined from $\tan \angle FAC = f_y/f_x$, where f_y and f_x are known design parameters (Table 3).

3.2. Calibration

Calibration is important for ensuring accurate HIFU treatment under the US image guidance. To locate the target region in the workspace of the treatment system from the diagnostic image, we need the spatial relation between the US image space and the robot workspace. Denoting the coordinate system of the US image as $\{U\}$ (in pixels) and those of the robot base as $\{B\}$ (in mm), we seek the relative pose ${}^B\xi_U$ describing $\{U\}$ with respect to $\{B\}$. This relation is given by Eq. (5):

$$\begin{bmatrix} {}^Bx \\ {}^By \\ {}^Bz \\ 1 \end{bmatrix} = {}^B\xi_U \cdot \begin{bmatrix} u \\ v \\ 0 \\ 1 \end{bmatrix} \quad (5)$$

where ${}^B\mathbf{p} \sim [{}^Bx, {}^By, {}^Bz, 1]^T$ is the homogeneous position representation of an arbitrary point on the image plane in $\{B\}$, and ${}^U\mathbf{p} \sim [u, v, 0, 1]^T$ is the homogeneous position representation of the same point on a 2D US image. The transformation matrix ${}^B\xi_U$ is resolved by the following procedures:

(1) To simplify the calculation, the original image-coordinate system $\{U\}$ (in pixels) is transformed into a new image-coordinate system $\{I\}$ (in mm). The transformation ${}^I\xi_U$ scales $\{U\}$ along the u and v directions with factors s_u and s_v , respectively, shifts the origin by a translation, and adjusts the axial direction by a rotation.

(2) The image-coordinate system $\{I\}$ is transformed into a reference coordinate system in a 3D space that is fixed with respect to a world coordinate system. The transformation is performed by imaging a phantom with known geometric properties. The phantom coordinate system is denoted as $\{P\}$.

(3) The image-coordinate system $\{I\}$ is registered with the robot end-effector coordinate system $\{E\}$. The pose of the end-effector in the robot base $\{B\}$ is read from the robot encoders output. $\{I\}$ and $\{E\}$ are related through $\{P\}$ and an external tracking system that provides a world coordinate system $\{G\}$ as the reference.

Therefore, the problem is solved as follows:

$${}^B\xi_U = {}^B\xi_E \cdot {}^E\xi_G \cdot {}^G\xi_P \cdot {}^P\xi_I \cdot {}^I\xi_U \quad (6)$$

The scaling factors s_u and s_v in ${}^I\xi_U$ are determined from the display information of the diagnostic US instrument, specifically, by counting the numbers of pixels along the u and v directions, respectively, corresponding to the length indicated by the scale bar. The translation and rotation transformations are performed only for computational convenience, so these parameters are already known. Consequently, we can obtain ${}^I\xi_U$. As the pose of the end-effector is read from the encoders, ${}^B\xi_E$ is also known. The problem then simplifies to Eq. (7):

$${}^E\xi_I = {}^E\xi_G \cdot {}^G\xi_P \cdot {}^P\xi_I \quad (7)$$

${}^P\xi_I$ is determined by the N-fiducial phantom method described in Refs. [11] and [12]. The custom-made phantom is shown in Fig. 6. The “N” shape was formed by a fishing-line wire with diameter $\phi = 0.2$ mm. The world coordinate (reference) system $\{G\}$ is provided by an external optical tracking system (Polaris Spectra®,

Northern Digital Inc., Waterloo, ON, Canada). G_{ξ_p} is obtained by localizing the marker points on the custom-made phantom using the pen-tool of the optical tracking system. G_{ξ_E} is resolved by localizing the sampling points on several faces of a custom-made probe holder, which fixes the US imaging transducer on the end-effector. The inverse computation gives E_{ξ_G} , the final parameter to be determined in Eq. (6).

3.3. Evaluation of the calibration accuracy

The calibration accuracy was evaluated by the linear scanning of another wire phantom with known geometry, and by comparing the features of the 3D-reconstructed US image with the physical measurements. Related methods are described in Refs. [13] and [14]. The calibration accuracy was evaluated on the phantom shown in Fig. 7(a), which consists of two layers of wires. Fig. 7(b) is a US image of the wire grids. The phantom coordinate system is denoted as $\{Q\}$. The line interval is 6.0 mm along the x_Q axis and 5.0 mm along the y_Q axis. The wires on each layer form an 11-by-9 grid with 99 intersections. The phantom contains several holes, whose positions are localized in the world coordinate system $\{G\}$ of the optical tracking system using the pen-tool in order to obtain the spatial relation G_{ξ_Q} . Therefore, the phantom coordinate system $\{Q\}$ is registered with the robot base coordinate sys-

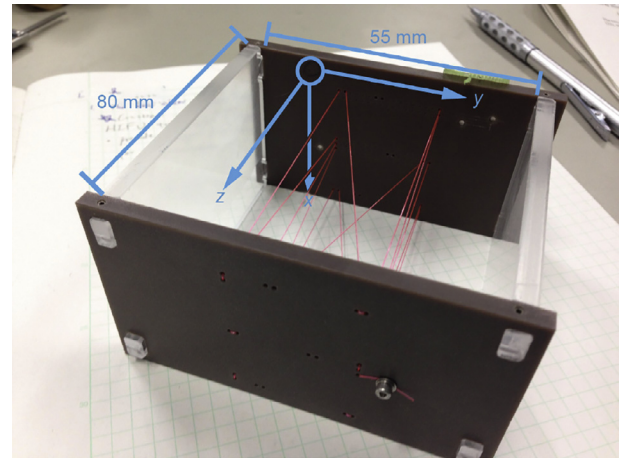


Fig. 6. The N-fiducial phantom for calibration.

tem $\{B\}$ as $B_{\xi_Q} = B_{\xi_E} \cdot E_{\xi_G} \cdot G_{\xi_Q}$, and the positions of all intersections are known in $\{B\}$. Next, the 3D US image of the phantom is segmented by thresholding, and each wire string is classified by data brushing (Fig. 8(a)). Each set of brushed data is

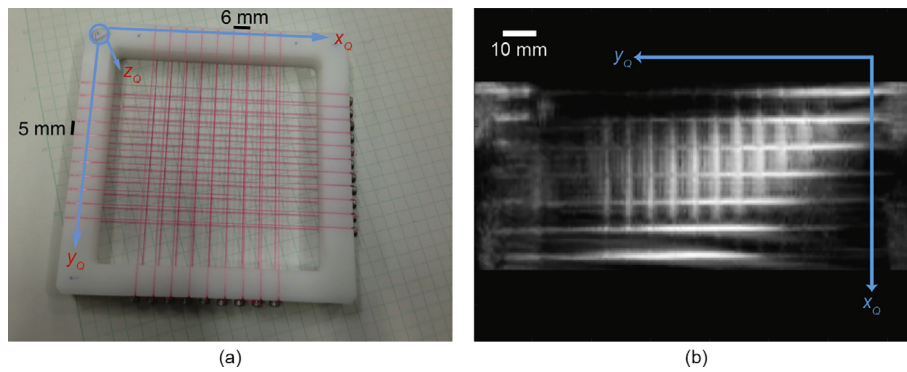


Fig. 7. (a) Photograph and (b) US image of the parallel-wire phantom used in the calibration evaluation.

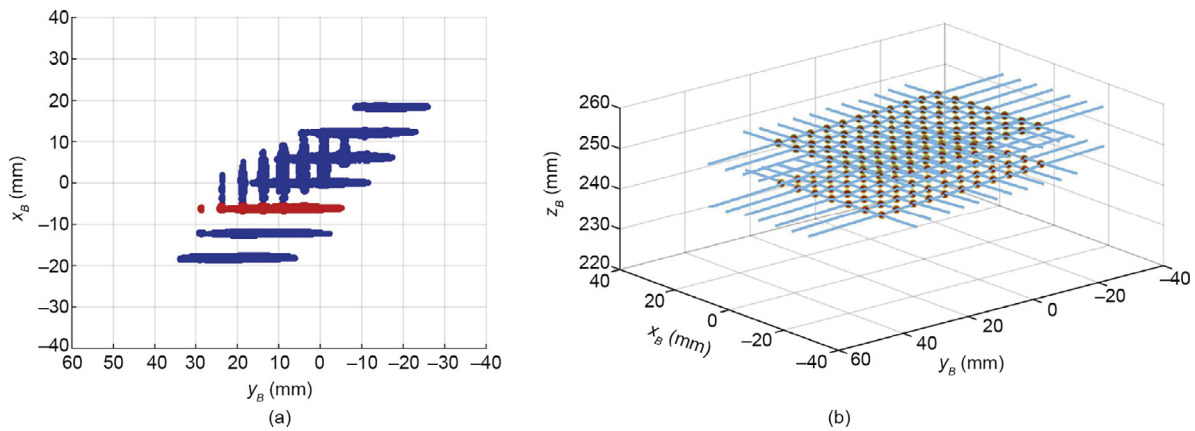


Fig. 8. Processing of the US images by (a) brush classification of the wire data, where the blue points are all wires segmented from thresholding, and the red points are user brushed data points that belong to a single wire, and (b) linear fitting of the classified data.

independently fitted by a straight line in a 3D Euclidean space, \mathbb{R}^3 (Fig. 8(b)). We then calculate the positions of the line intersections. Finally, to validate the calibration, we compare the absolute positions of the intersections obtained from the 3D US image with the actual positions obtained from the measurements by the optical tracking system.

3.4. 3D US image reconstruction

3D US images reveal both the targets and their surrounding contexts, thus allowing intuitive exploration of the diagnosis region. Various methods that reconstruct 3D US images from multiple 2D image frames are available [15]. Unlike freehand 3D US reconstruction, given the hand-eye relation our robot-based navigation system plans the scan path precisely, without requiring an external tracking device. In our system, the images are gathered by a frame grabber as the robot linearly scans its y axis, and are transferred to the personal computer, where they are reconstructed by a voxel-based method. Each voxel in the 3D image is indexed as (i, j, k) , and the position of an arbitrary pixel in the 2D image stack is represented by (u, v, f) , where f is the frame index. The reconstruction and its algorithm are presented in Fig. 9(a) and the Appendix, respectively. Fig. 9(b) shows the relative orientation of the volume grid in the robot base coordinate system $\{B\}$. Each voxel is assigned a value from the interpolation between several appropriate 2D image pixels.

The reconstructed 3D US image is visualized in three orthogonal planes (i.e., the coronal view, the transverse view, and the sagittal view). The reconstruction is easily explored using a mouse.

3.5. Segmentation

To define the target region of the HIFU treatment, the tumor area must be segmented from its surroundings. Automatic segmentation is difficult because the US image is granulated by speckle effects. Although manual segmentation is possible under any conditions, manually segmenting a large number of images places an unreasonable workload on the surgeon. To ease the burden of segmentation for 2D planes, our system adopts an interactive assisted tool called Livewire [16]. As the surgeon moves the cursor on a grayscale US image, the local costs to neighboring pixels are calculated as the process continues. When the user clicks the mouse, an anchor point for calculating the new local costs is

determined, and the previous automatically generated local path becomes fixed. The target region is segmented after several clicks. In practical treatment, several planes must be segmented to extract the 3D volume of the tumor. In this paper, we evaluate the treatment accuracy on a single 2D plane.

3.6. Treatment path generation

After segmenting out the target region, we must generate a path by which the robot manipulates the HIFU transducer to perform the treatment. For this purpose, we require two kinds of parameters. First, we must determine the planned spot positions of the HIFU treatment in the robot base coordinate system. Second, we must determine the orientation of the HIFU beam on each spot. In contrast to the MRI-guided system, the orientation directions in the gantry are very limited for HIFU treatment. Our system removes this spatial limitation for the first time, and realizes a highly flexible HIFU treatment from various orientations.

The spatial information of a single planned treatment spot includes the spot position and the beam direction to the spot. These parameters are described by the $(\theta, x, y, z, \varphi)$ parameters of the robot. The parameters (θ, φ) define the azimuth and elevation angle of the beam, respectively (i.e., the beam orientation), while (x, y, z) define the position of the HIFU focal point. Therefore, the treatment execution requires a sequence of robot poses $\xi_i \sim (\theta_i, x_i, y_i, z_i, \varphi_i)$ (for $i = 1, 2, 3, \dots, n$), and the HIFU irradiation conditions (i.e., the power, duration, and cooling-time settings).

To treat the target region delineated by the segmentation results, the surgeon first determines the treatment plane; that is, the 2D plane of the target on which to place the treatment spots. The number of treatment planes (one or several) depends on the volume of the target. As a safety margin, the amount of surrounding tissue in the target region can be varied by expanding or shrinking the target contours. The target region is uniformly gridded and filled with treatment spots. The user then sets the beam direction. For versatile treatment at a single treatment point, the robot system can irradiate the HIFU from different directions. In the anticipated usage of the robot system, the patient will lie prone above the water tank. Therefore, we simplify the process by setting the treatment plane parallel to the coronal plane and fixing the beam direction perpendicular to the coronal plane. The experimental setup is illustrated in Fig. 10. (A breast-shaped phantom is appropriately placed in the system workspace.)

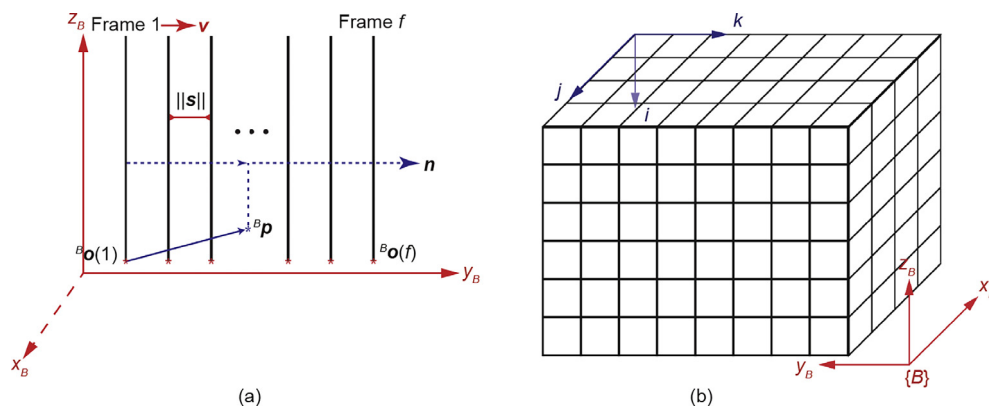


Fig. 9. (a) Linear scan process in 3D US image reconstruction (\mathbf{v} is the speed vector of the scan; \mathbf{n} is the normal vector of the 2D US image frame; $\|s\|$ is distance between successive frames; ${}^B\mathbf{o}(1)$ is the origin of the first frame, while ${}^B\mathbf{o}(f)$ is the origin of the f th frame); (b) the voxel data grid of the 3D US image.

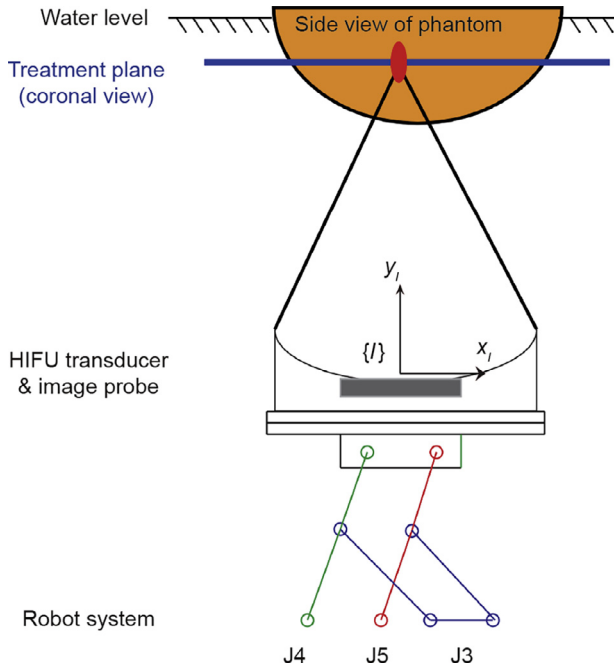


Fig. 10. Path generation with fixed orientation. The blue line, red spot, and gray box indicate the treatment plane, the HIFU focal point, and the US imaging probe, respectively.

3.7. System evaluation method

The US-guided robot-assisted HIFU treatment system was evaluated in an experiment that simulated the clinical treatment. We designed a heterogeneous phantom comprising a simulated tumor, surrounding normal tissue, and markers. Fig. 11(a) and (b) present a schematic of the phantom design and a photograph of the pre-

pared phantom, respectively. The phantom was constructed from transparent acrylamide gel containing degassed, diced chicken meat and pieces of porcine liver. The chicken meat represented the tumor region to be treated, while the surrounding porcine liver represented the normal tissue. Four reference markers provided a physical coordinate system for evaluating the treatment performance. The marker positions were determinable both on the US image during the treatment planning and on the photograph during the post-treatment analysis. The markers provided a spatial reference for relating the separate domains of the US image, the optical photograph, and the physical space.

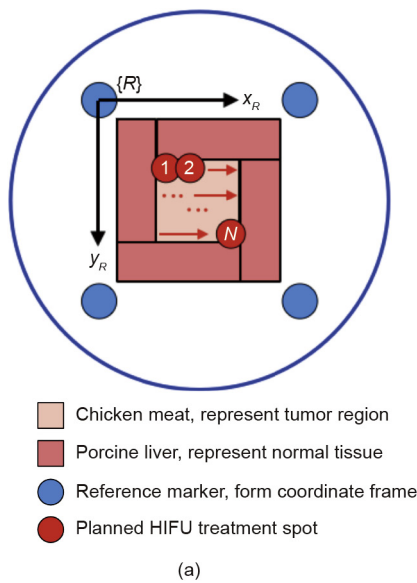
The evaluation was quantified by the absolute deviation between the planned and actual treated regions, the completion degree of the treatment, and the overshoot around the planned region. The experimental procedure is summarized below.

- (1) Reconstruct the 3D US image of the phantom from the 2D US frames collected during linear scans performed by the robot.
 - (2) Set the treatment plane close to the bottom surface of the chicken meat (the surface that is closer to the HIFU transducer).
 - (3) Segment the target region (i.e., the chicken meat) from the surrounding tissue (i.e., the porcine liver).
 - (4) Fill the target region with planned HIFU treatment spots. The ablation area of a single HIFU treatment spot is estimated as a circle with a diameter of 5.0 mm. The interval between treatment spots is 3.5 mm.
 - (5) Export the treatment path information to the robot system and execute the HIFU irradiation.
 - (6) Evaluate the US-guided HIFU treatment by comparing the actual and planned treated regions.
- The evaluation method is detailed in Ref. [17].

4. Results

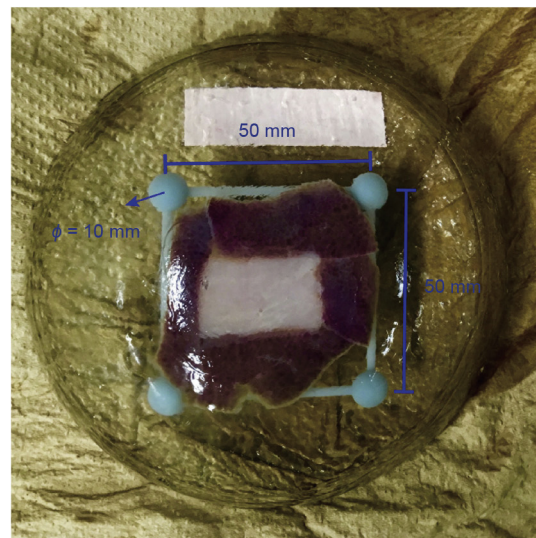
4.1. Calibration results

The calibration experiment included 18 independent trials with different absolute poses of the end-effector or the N-fiducial



- Chicken meat, represent tumor region
- Porcine liver, represent normal tissue
- Reference marker, form coordinate frame
- Planned HIFU treatment spot

(a)



(b)

Fig. 11. (a) Schematic and (b) photograph of the heterogeneous phantom that was used for system evaluation. The markers are designed that they can provide a Cartesian reference coordinate system $\{R\}$.

Table 4
Calibration results of 18 independent trials.

No.	Roll (°)	Pitch (°)	Yaw (°)	T_x (mm)	T_y (mm)	T_z (mm)
1	-90.5	-2.7	179.2	-0.4	-1.9	33.8
2	-91.9	-0.4	180.3	0.3	-4.2	33.7
3	-93.9	3.4	179.5	-0.5	-4.4	33.7
4	-90.9	-2.1	179.9	-0.1	-3.6	33.5
5	-90.5	-2.3	179.7	0.1	-3.2	33.6
6	-89.2	0.2	179.6	-0.2	0	33.3
7	-89.9	1.3	179.8	0	-1.3	33.9
8	-89.3	1.1	179.6	0.2	-1.7	33.4
9	-89.5	2.0	179.2	-0.0	0.6	33.1
10	-90.3	-2.9	179.8	-0.1	-1.8	33.1
11	-88.6	-3.6	180.0	-0.3	-0.3	32.7
12	-90.1	3.1	179.6	-0.7	-0.7	33.5
13	-91.2	2.7	180.0	-0.4	-2.7	33.9
14	-89.0	-2.2	179.9	-0.1	-1.2	33.1
15	-88.6	-3.1	180.1	-0.3	-1.1	33.7
16	-88.1	2.3	179.5	0.4	1.0	34.1
17	-87.8	1.1	180.1	0.9	-1.0	33.5
18	-89.0	0.8	180.4	-1.2	-1.4	33.6
Mean	-89.9	-0.1	179.8	-0.1	-1.6	33.5
STD	1.5	2.4	0.4	0.5	1.6	0.4

STD: standard deviation.

phantom. Table 4 shows the calibrated transformation matrix ${}^E\xi_I$. Each row represents the relative pose of the US image-coordinate system $\{I\}$ with respect to the robot end-effector coordinate system $\{E\}$, calculated in a single trial. The rotation part of the transformation matrix adopts the roll, pitch, and yaw angle convention (i.e., successive rotation about the x , y , and z axes), and the translation part specifies the translations along the x , y and z axes (denoted by T_x , T_y , and T_z accordingly). The final result is the mean of the 18 trials.

4.2. Accuracy of calibration

Owing to the limited imaging width, the system imaged only 77 out of 99 intersections in the bottom layer of the phantom (the one that is closer to the imaging transducer), and 88 out of 99 intersections in the upper layer. Table 5 presents the mean differences between the intersection positions obtained from the 3D US image and those obtained based on the measurements by the optical tracking system. Here, Δx , Δy , and Δz denote the displacements in the x_B , y_B , and z_B directions, respectively. The absolute deviations were calculated as $\Delta d = \sqrt{\Delta x^2 + \Delta y^2 + \Delta z^2}$. The measured intersections were assumed as the benchmark values. On average, the positions obtained from the 3D US image matched the benchmark positions within 2 mm.

4.3. System evaluation results

Next, the US-guided HIFU treatment was evaluated three times on the heterogeneous phantom. The results of the three trials are shown in Fig. 12. The subfigures in columns (a), (b), and (c) respectively show the treatment plan on the US image, the actual treated region after the HIFU irradiation, and a comparison of the

Table 5
Evaluation results of the calibration.

	Δx (mm)	Δy (mm)	Δz (mm)	Δd (mm)
Mean	-1.6	0.7	-0.2	1.8
STD	0.3	0.3	0.2	0.3

planned and actual treated regions registered to the same coordinate system $\{R\}$ provided by the reference markers.

The statistics of the planned and actual treatment regions are listed in Table 6. The area ratio of the untreated to the planned treatment region was quantified by the false-negative rate (FNR), defined as follows:

$$\text{FNR} = \frac{|P - A \cap P|}{|P|} \quad (8)$$

where $|P|$ and $|A|$ are the planned and actual treated regions, respectively. The overshoot is calculated by transforming the planned and actual treated regions into the same polar coordinates, and calculating their radial differences. The overshoot results are expressed by their means and standard deviations.

In trials 1 and 2, the actual HIFU ablation area fully covered the planned region. In trial 1, the centroids of the planned and actual ablation areas differed by 0.3 mm, and the overshoot around the planned region was approximately (1.5 ± 1.0) mm. In trial 2, the centroid deviation was 0.9 mm and the overshoot around the planned region was approximately (4.2 ± 1.9) mm. In trial 3, 0.5% of the planned region was not covered by the actual ablation area. The centroids of the planned and actual ablation areas differed by 1.1 mm and the overshoot around the planned region was approximately (2.6 ± 1.5) mm. These results are discussed in the next section.

5. Discussion

In the system development described above, we constructed and integrated the functional blocks of 3D US image reconstruction, image segmentation, and path generation of the executed treatment. However, several functional blocks need to be improved. The current 3D reconstruction method performs only one scan. Given the limited field of view of the imaging probe, part of the object area may be omitted. The view region could be expanded by a volume-compounding method that conducts multiple scans. Adjusting the beam direction, tuning the distribution of treatment spots, and other refinement functionalities would enable a more detailed treatment planning.

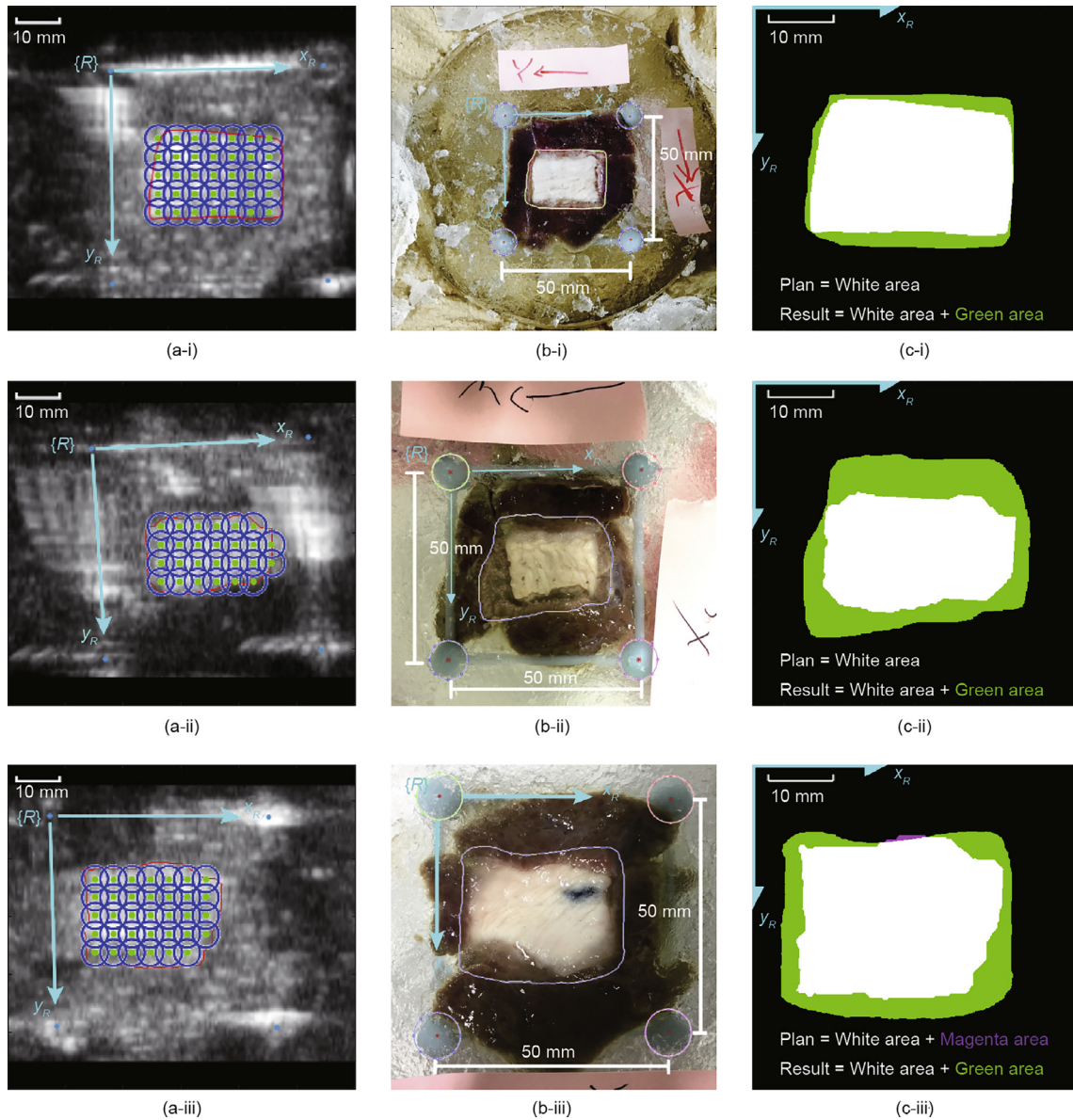


Fig. 12. Results of the system evaluation experiments. Rows (i), (ii), and (iii) correspond to trails 1, 2, and 3, respectively. In column (a), the red lines enclose the planned region of the HIFU treatment; the blue circles and green dots indicate the estimated ablation areas and positions of the individual HIFU spots, respectively. In column (b), the closed curves bounding the chicken meat delineate the visually identified actual treated region, the four circles on each image are used to help calculating the center of the markers in image space. In column (c), the planned region for each trail is colored with white, the over-treated region is colored with green, while the untreated are is colored with magenta.

Table 6
Statistics of the accuracy evaluation.

Experiment		Area (mm ²)	Centroid (mm)	Centroid deviation (mm)	FNR (%)	Degree of completion (%)	Overshoot (mm)
Trial 1	Plan	591.1	(24.5, 25.3)	0.3	0	100.0	1.5 ± 1.0
	Result	716.2	(24.6, 25.6)				
Trial 2	Plan	458.6	(25.2, 26.2)	0.9	0	100.0	4.2 ± 1.9
	Result	822.7	(25.1, 25.3)				
Trial 3	Plan	678.5	(22.2, 23.7)	1.1	0.5	99.5	2.6 ± 1.5
	Result	950.7	(22.3, 24.8)				

In the system evaluation experiments, the centroids of the planned region deviated from the centroids of the HIFU-ablation area by less than 2 mm. The relatively large overshoot in trial 2

might be attributable to partial liver damage during the phantom preparation, as the coagulating gel releases a considerable amount of heat. The different overshoot areas in the three experiments

probably reflect variations in the phantom preparation process, which may introduce air bubbles (leading to cavitation). In trial 3, the incomplete coverage of the planned region indicates a lack of safety margin setting. During the experiments, the planned treatment region was assumed to equal the segmented region of the chicken meat (i.e., equivalent to a safety margin of 0 mm). This area was filled with HIFU focus spots with estimated ablation areas.

However, the actual ablation area of a single HIFU focus spot may vary among cases. In clinical treatment applications, surgeons usually allow a 10 mm safety margin to ensure complete treatment [18]. From this viewpoint, the current overshoot is well below the tolerance and our system is sufficiently accurate. In future study, the proper safety margin should be determined in further experiments, and the phantom preparation process should be more rigorously controlled.

The phantom designed for the evaluation experiment determines the accuracy of the US-guided HIFU treatment on a 2D plane, but cannot precisely evaluate the accuracy along the axial direction of the HIFU beam. However, under the conditions of our experiments, a single HIFU focus spot is approximately 10 mm long in this direction, meaning that a single treatment plane will treat a volume with a thickness of ~ 10 mm. Therefore, in practical breast cancer treatment, only a few treatment planes are needed. Our method could be extended to multiple treatment planes and the accuracy could be estimated on the treatment volume instead of the treatment area.

Moreover, the phantom used in the present evaluation lacks a component mimicking the skin of the breast. Consequently, we cannot measure the refractive deviation of the HIFU focus when the beam is irradiated non-orthogonally to the skin surface. In future work, the focal deviation will be assessed on a more realistic phantom with a component that mimics breast skin.

The current experiment assumed a constant speed of sound. Our system can maintain the HIFU focus point fixed in space while changing the approach direction of the beam. This novel configuration reduces the risk of skin burn. However, the inhomogeneity of biological tissue will generate an inhomogeneous distribution of sound speeds, so the actual HIFU focus spot will deviate from the planned position. We anticipate that our heterogeneous phantom will reveal the error caused by the inhomogeneous sound speeds, because the actual treated region can always be directly compared with the planned region.

In the current evaluation experiments, the HIFU irradiation power and its duration were both constant. In further research, the power and irradiation time of each shot will be adapted to the shape of the target region. This will improve the accuracy of the treatment and minimize the damage to normal tissue. Moreover, in this paper, the position of the HIFU treatment spot was only controlled by the robot system. In future, we plan to electronically focus the HIFU beam in order to fine-tune the position of the focus spot.

6. Conclusions

We presented a US-guided, five-DOF robot-assisted HIFU treatment system for breast cancer. A fully functional prototype allowing easy 3D reconstruction of US images, target segmentation, treatment path generation, and automatic HIFU irradiation has been constructed. The system was evaluated on a heterogeneous tissue phantom. The centroids of the planned treatment region and the HIFU ablation area deviated within 2 mm, and the

overshoot around the planned region was well below the tolerance of clinical usage. The accuracy was considered to be sufficient for complete treatment, given that surgeons set an over-treatment margin. In future work, the system should be improved by increasing the flexibility of the treatment plan, and the treatment accuracy should be evaluated in 3D space. The effects of inhomogeneous sound speed induced by tissue inhomogeneity should also be considered.

Acknowledgments

This work was partially supported by the Translational Systems Biology and Medicine Initiative (TSBMI) from the Ministry of Education, Culture, Sports, Science and Technology (MEXT) of Japan. The authors would also like to thank the China Scholarship Council and Otsuka Toshimi Scholarship Foundation.

Compliance with ethics guidelines

Tianhan Tang, Takashi Azuma, Toshihide Iwahashi, Hideki Takeuchi, Etsuko Kobayashi, and Ichiro Sakuma declare that they have no conflict of interest or financial conflicts to disclose.

Appendix A. Supplementary data

Supplementary data associated with this article can be found, in the online version, at <https://doi.org/10.1016/j.eng.2018.07.008>.

References

- [1] American Cancer Society, Inc. *Global cancer facts & figures*. 3rd ed. Atlanta: American Cancer Society, Inc.; 2015.
- [2] Japanese Breast Cancer Society. *Report of clinical statistical studies on registrated mammary cancer patients in Japan*. Tokyo: Japanese Breast Cancer Society; 2011. Japanese.
- [3] Kennedy JE. High-intensity focused ultrasound in the treatment of solid tumours. *Nat Rev Cancer* 2005;5(4):321–7.
- [4] Smith NB, Temkin JM, Shapiro F, Hynynen K. Thermal effects of focused ultrasound energy on bone tissue. *Ultrasound Med Biol* 2001;27(10):1427–33.
- [5] Furusawa H. High-intensity focused ultrasound for breast cancer: MR-guided focused ultrasound surgery as local treatment. *Choonpa Igaku* 2014;41(5):705–15. Japanese.
- [6] Ishihara Y, Calderon A, Watanabe H, Okamoto K, Suzuki Y, Kuroda K, et al. A precise and fast temperature mapping using water proton chemical shift. *Magn Reson Med* 1995;34(6):814–23.
- [7] Sherar MD, Moriarty JA, Kolios MC, Chen JC, Peters RD, Ang LC, et al. Comparison of thermal damage calculated using magnetic resonance thermometry, with magnetic resonance imaging post-treatment and histology, after interstitial microwave thermal therapy of rabbit brain. *Phys Med Biol* 2000;45(12):3563–76.
- [8] Yang B, Tan UX, McMillan AB, Gullapalli R, Desai JP. Design and control of a 1-DOF MRI compatible pneumatically actuated robot with long transmission lines. *IEEE ASME Trans Mechatron* 2011;16(6):1040–8.
- [9] Culjat MO, Goldenberg D, Tewari P, Singh RS. A review of tissue substitutes for ultrasound imaging. *Ultrasound Med Biol* 2010;36(6):861–73.
- [10] Yonetsuji T, Ando T, Wang J, Sakuma I. A novel high intensity focused ultrasound robotic system for breast cancer treatment. In: *Proceedings of MICCAI 2013: 16th International Conference on Medical Image Computing and Computer-Assisted Intervention*; 2013 Sep 22–26; Nagoya, Japan; 2013. p. 388–95.
- [11] Comeau RM, Fenster A, Peters TM. Integrated MR and ultrasound imaging for improved image guidance in neurosurgery. *Proc SPIE* 1998;3338:747–54.
- [12] Pagoulatos N, Haynor DR, Kim Y. A fast calibration method for 3-D tracking of ultrasound images using a spatial localizer. *Ultrasound Med Biol* 2001;27(9):1219–29.
- [13] Fenster A, Bax J, Neshat H, Kakani N, Romagnoli C. 3D Ultrasound imaging in image-guided intervention. In: *Proceedings of 2014 36th Annual International Conference of the IEEE*; 2014 Aug 26–30; Chicago, IL, USA. New York: IEEE; 2013.

- [14] Kim C, Chang D, Petrisor D, Chirikjian G, Han M, Stoianovici D. Ultrasound probe and needle-guide calibration for robotic ultrasound scanning and needle targeting. *IEEE Trans Biomed Eng* 2013;60(6):1728–34.
- [15] Solberg OV, Lindseth F, Torp H, Blake RE, Nagelhus Hernes TA. Freehand 3D ultrasound reconstruction algorithms—a review. *Ultrasound Med Biol* 2007;33(7):991–1009.
- [16] Mortensen EN, Barrett WA. Intelligent scissors for image composition. In: *Proceedings of the 22nd Annual Conference on Computer Graphics and Interactive Techniques*; 1995 Aug 6–11; New York, NY, USA. New York: ACM; 1995. p. 191–8.
- [17] Tang T, Azuma T, Itani K, Iwahashi T, Matsui K, Fujiwara K, et al. A new method for absolute accuracy evaluation of a US-guided HIFU system with heterogeneous phantom. In: *Proceedings of 2016 IEEE International Conference*; 2016 Sep 18–21; Tours, France. New York: IEEE; 2016. p. 1–4.
- [18] Zhou YF. High intensity focused ultrasound in clinical tumor ablation. *World J Clin Oncol* 2011;2(1):8–27.